ELSEVIER

Catalysis Today 77 (2002) 127–138

CATALYSIS TODAY

www.elsevier.com/locate/cattod

Catalytic activation of core-shell assembled gold nanoparticles as catalyst for methanol electrooxidation

Jin Luo [a], Mathew M. Maye [a], Yongbing Lou [a], Li Han [a], Maria Hepel [b], Chuan Jian Zhong [a,*]

[a] *Department of Chemistry, State University of New York at Binghamton, Binghamton, NY 13902, USA*
[b] *Department of Chemistry, State University of New York at Potsdam, Potsdam, NY 13676, USA*

Abstract

This paper describes the results of an investigation of the evolution and the reconstitution of core-shell assembled gold nanoparticles in electrocatalytic activation for methanol electrooxidation. The aim is to probe the structural and morphological reconstitution upon the catalytic activation. Gold nanoparticles of 2-nm core size are linked by 1,9-nonanedithiolates into a network thin film on planar substrate, and are explored as a model system of core-shell nanostructured catalysts. This system is probed using three characterization techniques: electrochemical quartz-crystal nanobalance (EQCN), infrared reflection spectroscopy (IRS), and atomic force microscopy (AFM). The EQCN detected two types of mass changes across the nanostructured catalysts. One corresponds to shell desorption upon the oxidative potential-driven activation, and the other relates to the formation of surface oxygenated species during the catalytic oxidation of methanol. IRS provided two pieces of evidence for the shell reconstruction upon the activation. One is indicative of the desorption of the shell thiolates, and the other relates to the interparticle electronic effect. AFM revealed morphological changes of the nanoparticle assemblies in terms of the film smoothness and the particle size that are dependent on the thickness of the nanoparticle assembly. While thick films displayed enlarged nanoparticle features, thinner films exhibited a relatively smaller evolution. The catalytic activity is associated with the partial or even complete desorption of network shell components accompanied by the formation of surface oxygenated species, a reconstitution process that may have important implications to the delineation of design and preparation parameters of nanoporous and highly active nanoscale catalysts.

Keywords: Catalytic activation; Shell reconstitution; Gold nanoparticles

1. Introduction

The development of highly active catalysts for fuel cells and the detailed mechanistic understanding have spanned from traditional platinum group catalysts to platinum-containing alloy catalysts and nanometer-size catalysts [1–4]. Extensive studies of catalysts for methanol oxidation have focused on the use of bimetallic (e.g. Pt–Ru) multi-component [5–8] and a variety of metal particles [9–13]. The effective preparation of nanoscale catalysts, the elimination of the propensity of poisoning at Pt-based catalysts, and the control of the tendency of nanoparticle aggregation remain, however, to be major challenging issues. Since the finding of high catalytic activity of nanosized gold less than 5 nm core sizes towards hydrocarbons and recent theoretical modeling of the unique properties of nanoscale gold [9,10], it is clear that to achieve highly active and stable gold catalysts

* Corresponding author. Tel.: +1-607-777-4605.
E-mail address: cjzhong@binghamton.edu (C.J. Zhong).

0920-5861/02/$ – see front matter © 2002 Elsevier Science B.V. All rights reserved.
PII: S0920-5861(02)00239-0

for CO oxidation requires a fortunate combination of factors and conditions, including size, support, and preparative route [12]. Although there is a growing experimental evidence showing the linkage of the catalytic activity to core sizes less than 5 nm, why, precisely, gold particles in such a restricted size range are catalytically active, is not yet clear [12,13].

Metallic (e.g. gold and alloy) nanocrystals capped in organic monolayer shells has recently emerged as an intriguing class of core-shell nanoparticles (CSN) [14,15]. The importance stems largely from the diverse attributes of CSN as model building blocks towards functional materials, including size-monodispersity, core- and shell-processibility, solubility, stability, capability of self-assembly, and reactivities involving optical, electronic, magnetic, catalytic and chemical/biological phenomena [14,16]. More importantly, such nanoscale building blocks can be viewed as new candidates of catalysts with size-tunable and aggregation- or poison-resistant catalytic properties. This motivation is inspired by the discovery of catalytic activities of gold particles in less than ~5 nm regime [9,10,17] and the abundant demonstration of core-shell reactivities of gold and alloy CSN [14,15,18]. While our recent findings have demonstrated that the core-shell assembled nanoparticles can be made electrocatalytically active towards the oxidation of CO [19] and methanol [20], how the nanosites are processed towards catalytically active and electrochemically accessible via the core-shell nanostructure manipulation is the central focus of the present work. The basic understanding will also be useful to much of the recent interest in oxide-supported gold catalysis and other similar nanoscale systems for catalysis. We note that the preparation of Pt/Ru colloidal catalysts using surfactant-stabilization route was recently reported for methanol oxidation fuel cell application [5b], which has demonstrated high catalytic activity. In the present paper, we discuss findings from characterizations of our core-shell nanostructured gold catalysts in the catalytic activation. We use planar substrates as the analytical platform for characterizations with an array of interfacial techniques such as electrochemical quartz-crystal nanobalance (EQCN) [21], atomic force microscopy (AFM), and infrared reflection spectroscopy (IRS).

2. Experimental section

2.1. Chemicals

The thiols used were decanethiol (DT, 96%) and 1,9-nonanedithiol (NDT, 95%). The gold compound was hydrogen tetracholoroaurate ($HAuCl_4$, 99%). The organic salts used were tetraoctylammonium bromide (TOABr, 99%). The reducing agent was sodium borohydride ($NaBH_4$, 99%). Other chemicals included toluene (99.8%), hexane (99.9%), methanol (99.9%), and ethanol (99.9%). All chemicals were purchased from Aldrich and used as received. Water was purified with a Millipore Milli-Q water system.

2.2. Synthesis of Au nanoparticles

Gold nanoparticles of 2-nm core size encapsulated with alkanethiolate monolayer shell ($Au_{2\,nm}$) were synthesized by standard two-phase method [15]. Briefly, $AuCl_4^-$ was first transferred from aqueous $HAuCl_4$ solution (10 mM) to toluene solution by phase transfer reagent TOABr (36 mM). Thiols, e.g. DT, were added to the solution at a 2:1 mole ratio (DT/Au), and an excess (12×) of aqueous $NaBH_4$ was slowly added for the reaction. The produced DT-encapsulated Au nanoparticles (~1.9 nm) were subjected to solvent removal and multiple cleanings using ethanol.

2.3. Preparation of Au_{2nm} film

Details of the preparation of the Au nanoparticle film formation are described elsewhere [22] and the general procedure is briefly summarized as follows.

Using 1,9-nonanedithiol (NDT) as crosslinking agent, the nanoparticles were assembled on a substrate electrode surface as an ensemble of the shell-linked particles via an exchange–crosslinking–precipitation route [20]. Briefly, a substrate electrode (glassy carbon disk or gold film slide) was immersed into a hexane solution of DT-capped nanoparticles (30 μM) and NDT (50 mM) for 4–24 h. During the immersion, the NDT–DT exchange reaction was followed by crosslinking, leading to nucleation and growth of a nanoparticle thin film on the substrate, i.e. NDT–$Au_{2\,nm}$. The thickness of the film was controlled

by immersion time. The films were thoroughly rinsed with the solvent and dried under argon. Films ranging from 1 to 20 eq. number of particle layers were estimated from quartz-crystal microbalance measurements [22b].

Several types of substrates were used for the thin film preparation. Glassy carbon (GC) disks (geometric area: 0.28 cm^2), polished with 0.03 μm Al_2O_3 powders, were mainly used for electrochemical and AFM measurements. Gold thin films evaporated on Cr-primed glass slides were used as substrates for infrared reflectance spectroscopic characterization. The surfaces were pre-cleaned by immersion in 1:3 H_2O_2 (30%)–H_2SO_4 (conc.) solution and rinsing in deionized water and ethanol. (**Caution: the H_2O_2–H_2SO_4 solution reacts violently with organic compounds and should be handled with extreme care.**) For EQCN experiments, 10 MHz gold-coated quartz-crystal piezoelectrodes (geometric area: 0.20 cm^2 for mass measurement and 0.23 cm^2 for current measurement) were used as substrates.

2.4. Instrumentation

An electrochemical quartz-crystal nanobalance setup was employed for measurements of cyclic voltammetric curves and EQCN curves [21]. It was composed of a microcomputer controlled potentiostat (Model PS-1705, ELCHEMA) and EQCN-900 instrument (ELCHEMA). The error limit of the mass detection is less than ±0.1 ng. The EQCN measurements were performed in the electrolyte solution purged with nitrogen at room temperature. All experiments were performed in three-electrode electrochemical cells. A saturated calomel electrode (SCE) was used as the reference electrode and a Pt coil was used as the counter electrode. All electrolytic solutions were deaerated with high purity argon or nitrogen before the measurement. All the potentials are quoted with respect to the saturated calomel electrode.

Infrared reflectance spectra (IRS) were acquired with a Nicolet 760 ESP FT-IR spectrometer that was purged with boil-off from liquid N_2. The spectrometer was equipped with a liquid nitrogen-cooled HgCdTe detector and a variable angle specular reflectance device. IRS measurements were performed in an external reflection mode using *p*-polarized light at an incident angle of 82° with respect to the surface normal. A gold slide coated with octadecanethiolate-d_{37} monolayer was used as the reference.

A Multimode NanoScope IIIa (Digital Instruments), equipped with an E scanner (maximum scan size: 16 μm), was utilized for imaging. The capability of TappingMode (TM)-AFM allows imaging at minimum disruption of the nanostructures. Standard silicon cantilevers (Nanoprobes) were used. The instrument was calibrated by imaging calibration using standard grating samples.

3. Results and discussion

The discussion of our experimental results is divided into three sub-sections. We first describe EQCN data to correlate the mass transport across the nanostructured catalyst film with the catalytic activation and activity. Secondly, we present surface IRS data to characterize the structural changes of the core-shell catalysts in the electrocatalytic activation. This sub-section is followed by the discussion of AFM data to characterize the morphological changes of the catalysts in the catalytic process.

3.1. EQCN measurement

The polarization of the catalyst-coated electrode by an anodic potential has been identified as a key process for the activation of the catalyst. We used EQCN to probe this activation process. Fig. 1A and B show a representative set of cyclic voltammetric EQCN data, i.e. current (A) and mass (B) change curves, for a NDT–$Au_{2\,nm}$ film during the catalytic activation process in an alkaline electrolyte. Based on the QCM measurement of frequency change corresponding to the mass loading of the film [22b], we estimated that this film consists of ∼17 eq. layers of linked nanoparticles, assuming a dense packing of the particles. Before activation of the film, i.e. in the first scan, there is no indication of methanol electrooxidation wave in the range of $E = +150$ to $+400$ mV (Fig. 1A), and the mass curves display almost featureless response up to $E = +400$ mV (Fig. 2B). With increasing number of cycles, it is evident that both the oxidation and the reduction currents increase (Fig. 1A). The anodic current

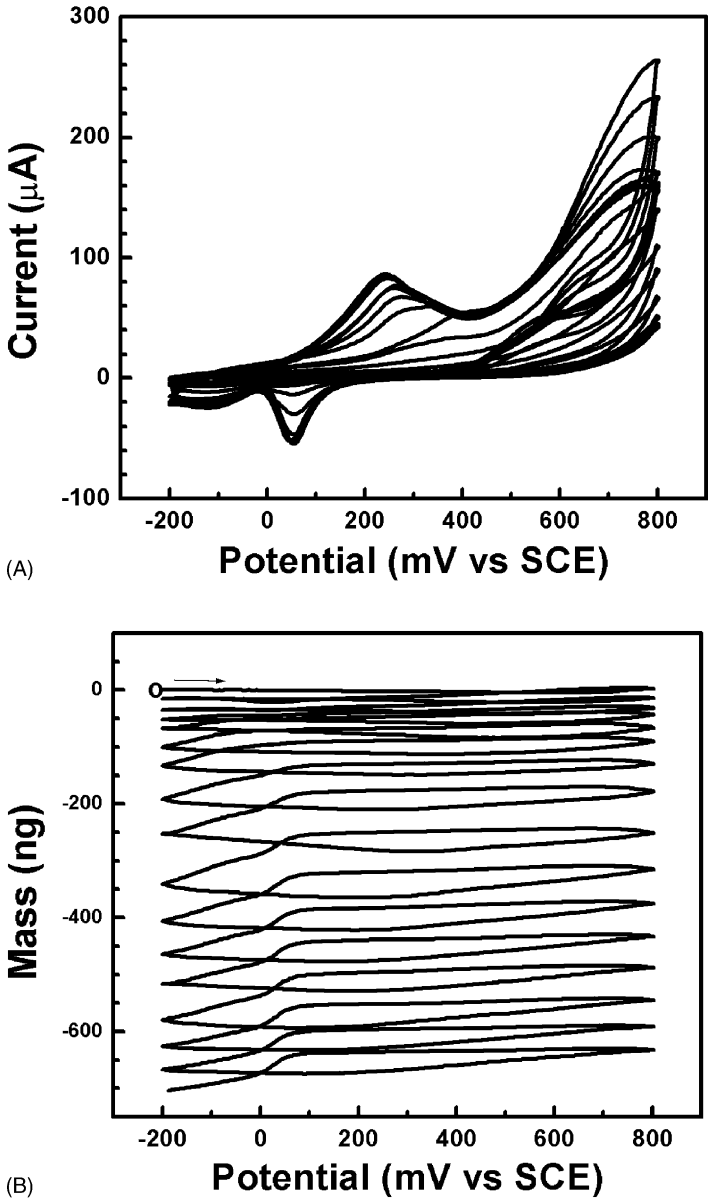

Fig. 1. (A) Current curve for an NDT–$Au_{2\,nm}$/EQCN electrode in electrolyte solution of 0.5 M KOH with 3.0 M methanol. Both anodic and cathodic currents increase with the number of cycling. (B) Mass curve for an NDT–$Au_{2\,nm}$/EQCN electrode in electrolyte solution of 0.5 M KOH with 3.0 M methanol. The mass decreases with the number of cycling. Scan rate: 50 mV/s.

wave appears around $E = +215$ mV, and the cathodic current wave appears at $E = +62$ mV. Significant changes of mass have been detected (Fig. 2B) accompanying the evolution of these voltammetric waves. Overall, the mass decreases gradually after each cycle, reaching about 700 ng, or 3500 ng/cm^2, after ~18 cycles.

If the detected mass decrease is assumed to be due to desorption of the networking thiolates, we can roughly estimate the expected mass change for

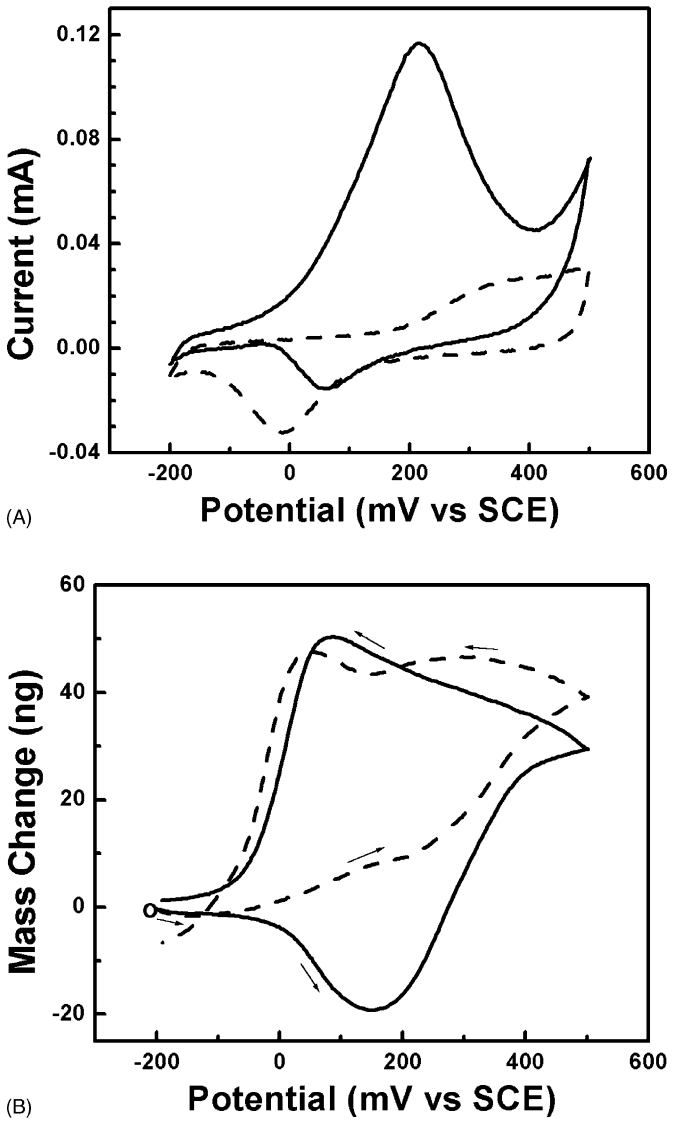

Fig. 2. (A) Current curve for an activated NDT–$Au_{2\,nm}$/EQCN electrode in electrolyte solution of 0.5 M KOH with (solid curve) and without (dash curve) 3.0 M methanol. (B) Mass curve for an activated NDT–$Au_{2\,nm}$/EQCN electrode in electrolyte solution of 0.5 M KOH with (solid curve) and without (dash curve) 3.0 M methanol. Scan rate: 50 mV/s.

the film under study, based on an idealized packing model [22,23].[1] The desorption of thiolates from 1 eq. layer would produce a mass change of 250 ng/cm^2. For the 17-layer film, the detected mass change corresponds to 80–90% of the thiolates in the film. It is important to note that the mass change depends on a number of factors, including core composition and thin film preparative conditions. For example, a gradual increase of the overall mass was detected for a film with Pt–Au alloy nanoparticles [20b]. While the

[1] For the estimate of the surface coverage of the NDT-linked $Au_{2\,nm}$ particles, a fully stretched *trans*-structure of alkyl chain is assumed, which gives 1.27 Å (–CH_2–), 1.8 Å (C–S bond), 0.71 Å (Au–S bond, projected), and ∠(Au–S–C) = 108°. This gives ∼1.5 nm for the interparticle distance (NDT). Relevant parameters are taken from the references [23].

detected mass increase could in general be attributed to the formation of surface oxygenated species and solvent uptakes during the catalytic activation [20b], we do not fully understand the mechanistic detail at this time. For the thin film catalysts consisting of Au nanoparticle cores, we consistently detected the gradual mass decrease as shown in Fig. 1B. A detailed assessment of the various factors is under way.

In addition to the gradual mass decrease during activation, fine structures of the mass change can be identified by examining the mass change profiles corresponding to the electrochemical oxidation and reduction waves developed after the catalytic activation. Fig. 2A and B compares the EQCN data of the activated NDT–$Au_{2\,nm}$ film (current and mass change, respectively) in solutions with and without methanol. In the positive potential sweep, the current curve displays an anodic wave at $E = +215$ mV in the solution with methanol (solid curve, Fig. 2A), which is attributed to methanol electrooxidation. This wave disappears (dashed curve, Fig. 2A) in the solution without methanol. The corresponding mass curve shows a wave in which the mass first decreases and then, increases (solid curve, Fig. 2B). The potential range of the mass wave slightly precedes the corresponding current wave. This feature is in contrast with the only increasing profile in the mass curve for the solution without methanol (dashed curve, Fig. 2B). This wave is, thus, believed to be linked to mass transport during methanol electrooxidation, possibly involving initial product release and the following formation of surface oxygenated species on the gold nanocrystals.

In the negative potential sweep, the current curve shows a cathodic wave at $E = +62$ mV, and the mass decreases at the same potential. In the solution without methanol, only a small wave of mass change was detected around $E = 300$ mV (dashed curve, Fig. 4). This wave is in part attributed to the reduction of gold associated with surface oxygenated species or oxides, and in part to the release of solvent or anions (OH^-) from the core-shell interface based on the character of the relative slow change in a wide-potential region.

Table 1 summarizes the above EQCN data in terms of the charges involved in the above processes. The charge under the anodic wave at $E = +215$ mV is about 1465 μC/cm^2, and the corresponding mass change is about 90 ng/cm^2. Since the anodic charge at $E = +215$ mV is much larger than the corresponding mass change upon translating the mass to charge, it follows that the charge is largely used in the oxidation process of methanol from the solution. For the reduction wave at $E = +62$ mV, the integrated charge is 164 μC/cm^2, corresponding to a charge for the reduction of 0.56 nmol/cm^2 coverage of $Au(OH)_3$. In comparison, the corresponding mass change is 235 ng/cm^2 (geometric area of the planar substrate). Since a monolayer coverage of oxygen on a planar surface is about 35 ng/cm^2, the amount of oxygenated species on the total nanocrystal surfaces of the assembled nanoparticles appears seven times more. A careful consideration of the actual surface areas of the 17-layer assembled particles, however, indicates that the assembly has a larger actual surface area (∼21 cm^2 per 1 cm^2 of geometric planar surface area). As such, the detected mass change is ∼2.3 ng/cm^2 after taking the actual total nanoparticle surface area into consideration. Based on a rough estimate of the molecular mass of the surface oxygenated species from the mass change and the charge for the gold oxide reduction in the absence of methanol (Fig. 2A, dashed curve), we found that it was suggestive of the possibility of $Au(OH)_3$ with about 10 water molecules which were released in the reduction process. This result could be due to an underestimate of the actual generation of oxide species in the presence of methanol. The electrogenerated oxide species were largely used in the electron mediation for methanol oxidation, as supported by the diminished reduction charge in the presence of methanol (Fig. 2A, solid curve). In the more positive potential region (+300 to +500 mV), the mass change reflects the further formation of surface oxygenated species which likely involves nanocrystals underneath the first oxide layer or at different depths of the nanoparticle layers. We believe a simultaneous formation of nanocrystal surface oxygenated species and electrocatalytic oxidation of methanol by the gold oxide species in the potential range is operative. The detected mass decrease

Table 1
EQCN data from Fig. 2

	Peak potential (mV)	Current charge (μC/cm^2)	Mass change (ng/cm^2)
Cathodic wave	Approx. +62	164	235
Anodic wave	Approx. +215	1465	90

for the reduction of the surface oxides appears to be only 6% of the mass estimated for a full monolayer coverage of oxide on all the nanocrystal surfaces in the nanoparticle assembly. This observation may be in part suggestive of the lack of a full surface coverage of gold nanocrystals by oxygenated species, and in part, indicative of the participation of the surface Au oxides as electron transfer mediators during the electrocatalytic oxidation of methanol. The former is qualitatively supported by the detection of alkyl components in the activated film, whereas the latter is consistent with the detection of reduction charge much smaller than the oxidation charge, as demonstrated in our previous electrochemical data [20a].

It is interesting to note that in the quick mass decrease region of the cathodic scan, the reduction wave of gold oxide species is shifted toward a more positive potential (∼70 mV) in the presence of methanol. While the course of this positive shift is not completely clear at this moment, two possible reasons may be considered: (i) reduced kinetic hindrance associated with increased permeability of the network nanostructure, or (ii) structural reconstitution via the formation of hydrated gold oxide species. Usually, the metal electrooxidation process begins with the formation of a hydrated metal oxide phase, which requires only proton transfer from the surface metal–water complex, e.g.

$$\mathrm{Au} + \mathrm{H_2O} - m\mathrm{e}^- = \mathrm{Au_2O_3} \cdot n\mathrm{H_2O}$$

or, in alkaline solution,

$$\mathrm{Au} + \mathrm{OH}^- - m\mathrm{e}^- = \mathrm{Au_2O_3} \cdot n\mathrm{H_2O}$$

where n is the number of hydrate molecules and m is the number of electrons.

In the next step, the hydrated oxide film may undergo dehydration, when this is a thermodynamically favorable process. However, for gold oxide, the hydration energy is negative, i.e. $\Delta G^{\circ}_{\mathrm{hydr}} = -7.53$ kcal/mol, which means that the dehydration process is not thermodynamically favorable. Because of the high methanol concentration in the catalyst activation process, the dehydration process may proceed. In this respect, methanol would act as a dehydrating agent. Note that the presence of methanol is crucial to the catalyst activation process. The resulting dehydrated surface oxide ($Au_2O_3 \cdot xH_2O$, where x accounts for the remaining hydration water molecules) should be reduced at more positive potential than the hydrated

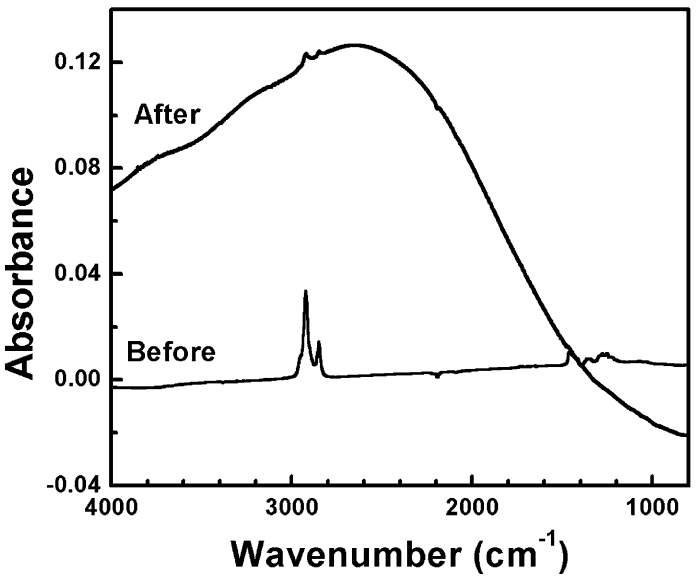

Fig. 3. IRS spectra for an NDT–$Au_{2\,nm}$ film before and after potential activation in an electrolyte solution of 0.5 M KOH with 3.0 M methanol. The spectral background for the entire spectral region is not corrected.

oxide, $Au(OH)_3$. The positive shift of the potential of surface gold oxide reduction is observed both in voltammetric and piezogravimetric characteristics. The expected equilibrium potential shift is

$$\Delta E_{eq} = \Delta E^0 = -\frac{\Delta G^{\circ}_{hydr}}{23.06n} = 0.054\,V,$$

where $n = 6$. This value is very close to the experimentally observed potential shift.

Overall, there is a clear distinction in the EQCN data between the presence of methanol and the absence of methanol after the catalytic activation. The formation of surface oxygenated species is believed to play an important role for the catalytic activity. In fact, the presence of the oxygenated species is detected using X-ray photoelectron spectroscopy, quantitative details of which will be reported elsewhere. In addition to the disappearances of the large oxidation current wave

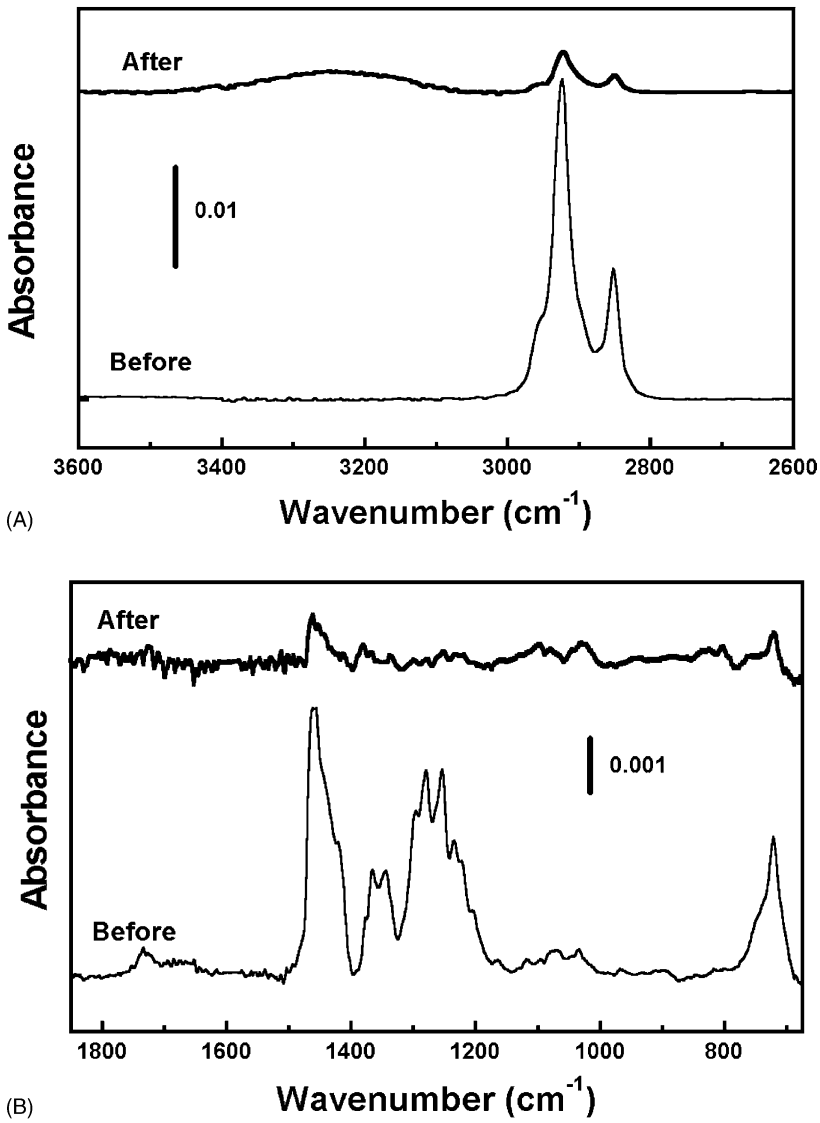

Fig. 4. IRS spectra after background correction of the data in Fig. 3: (A) in high-frequency region; (B) in low-frequency region.

and the initial mass decreasing feature in the positive potential sweep in the absence of methanol, the potentials for both the reduction current and the mass waves are about 15 mV (dashed curve, Fig. 2) more negative than that in the presence of methanol. While the exact origin is not clear at this time, we believe that the methanol-adsorption induced solvation of the nanostructured film may be partially operative.

3.2. IRS characterization

The structural information on the effect of the activation on the encapsulating structural properties is provided by IRS characterization. Fig. 3 presents a typical set of IRS spectra for the NDT–$Au_{2\,nm}$ film that compares the overall spectral feature before and after catalytic activation in the presence of methanol. These two spectra are compared with uncorrected spectral background. The activation process is exactly the same as described in the previous section. In Fig. 4A and B, the detailed spectral features of these spectra are compared with background-correction in both the high-frequency region (A) and the low-frequency region (B). These IRS data revealed two main pieces of evidence on the structural evolution of the core-shell nanoparticle assembly after catalytic evolution.

The first piece of evidence is about the desorption of the networking dithiolates by the activation, as characterized by the spectral features in the high-frequency region (Fig. 4A) that are diagnostic of the methylene stretching bands ($\nu_a(CH_2)$: ~2920 and $\nu_a(CH_2)$: ~2950 cm^{-1}) in the alkyl chains of NDT, and in the low-frequency region (Fig. 4B) that are diagnostic of C–H bending, wagging and C–C stretching modes [22a]. There is a clear reduction in absorbance for these bands after the catalytic activation. Although not completely disappeared, the significant reduction of these bands is suggestive of the removal of the shell NDT component from the nanostructured film, a result consistent with the EQCN-detected mass decrease upon catalytic activation described in the previous section. In addition, we detected a new and broad band in the 3200 cm^{-1} region. This observation is suggestive of the formation of hydrous species on the surface of the nanocrystal cores, a result in agreement with the formation of surface oxygenated species indicated by the EQCN data.

Secondly, the significant evolution in the spectral background before and after activation indicates that the interparticle property has been changed upon the catalytic activation. While the film exhibited a flat background before activation, the activated film showed a broad absorption band at ~2600 cm^{-1}. Qualitatively, this type of spectral evolution is characteristic of a conductive metallic absorption for the larger-sized particles in a continuous solid state [24]. Transmission NIR data were recently reported for thin films derived from 10 to 20 nm-sized bare gold particles via stepwise method [25]. Since the metallic inclusion in the insulative shell exhibits such surface plasmon absorption resonance in IR/NIR regions characteristic of network effect in a continuous film, we believe that the nanoparticles are densely packed after the removal of NDT, perhaps a certain degree of aggregation of the particles is also operative. In view of the formation of surface reconstitution from organic encapsulation to surface oxygenated species, we are also considering another possibility for the spectral evolution. The formation of the surface oxygenated species on the nanocrystal surfaces is expected to lead to effective isolation of the particle cores so that a finite band gap may exist.

3.3. AFM characterization

In the light of the structural reconstitution of the nanostructured film evidenced by the above EQCN and IRS data for the catalytic activation, we examined the morphological changes of the activated NDT–$Au_{2\,nm}$ films before and after the catalytic activation. Fig. 5 presents two representative sets of AFM images of two films with different thickness, ~7 layers (A) and ~3 layers (B). The film thickness was estimated from quartz-crystal microbalance measurement of the film mass loading and AFM measurement of the film cross-sections. The films were assembled on a polished glassy carbon substrate for the AFM imaging. Before activation (Fig. 5A(a) and B(a)), the assembled nanoparticles show generally a rough morphology with individually-isolated character. The apparent inhomogeneity feature of the overall surface morphology is partly due to the surface roughness effect of glassy carbon substrate. It is evident that the thinner film exhibits smoother and a higher degree of dispersion of the particles. The particles appear

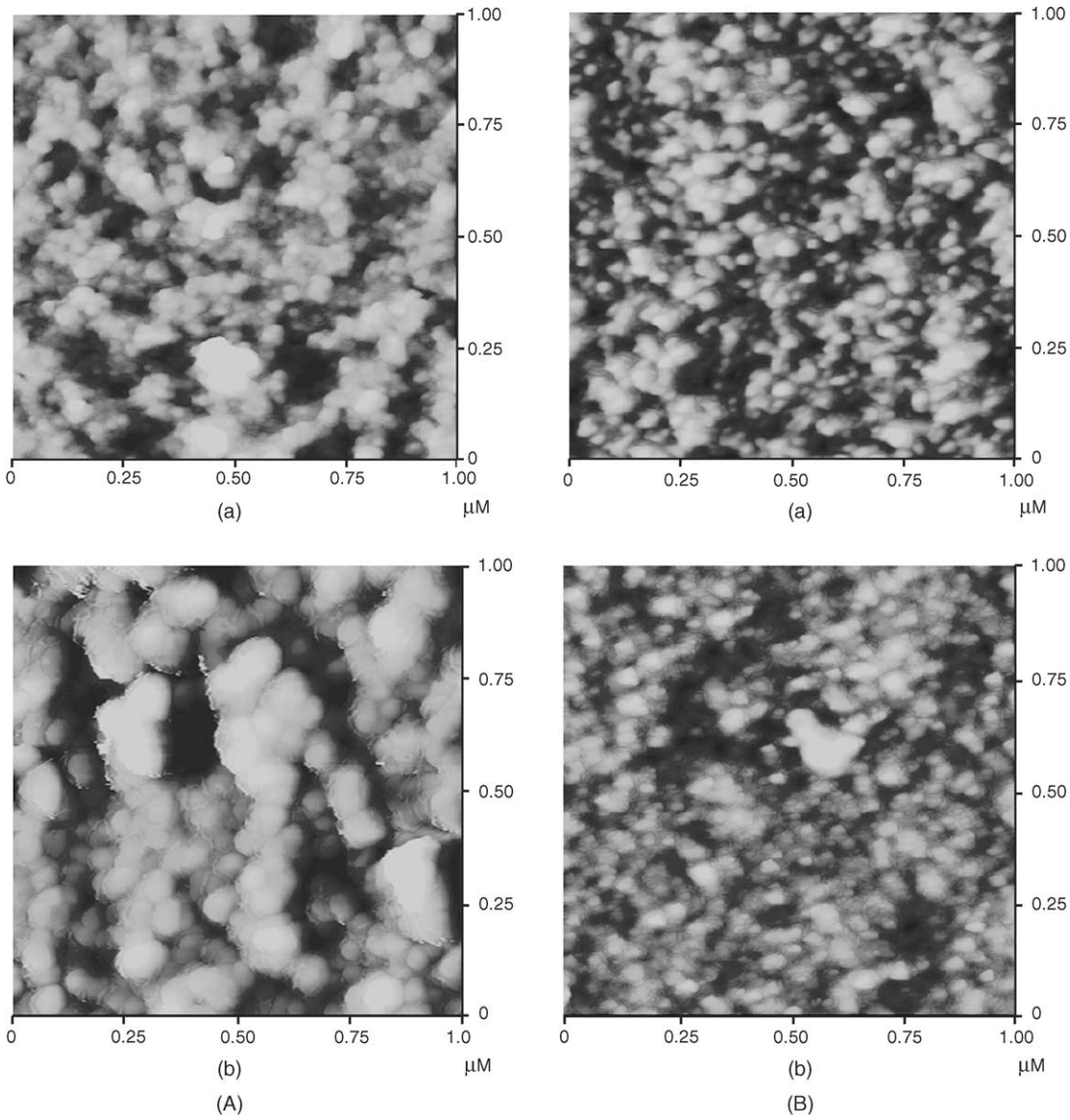

Fig. 5. TM-AFM images for NDT–$Au_{2\,nm}$/GC electrodes before (a) and after (b) potential activation in an electrolyte solution of 0.5 M KOH with 3.0 M methanol. (A) A thicker film (a and b): equivalent to ∼7 layers of nanoparticles; (B) A thinner film (a and b): equivalent to ∼3 layers of nanoparticles.

somewhat larger than the core-shell particle size due to tip–sample convolution and roughness effect of the glassy carbon surface, but the cross-section view reveals an average height as expected for the particle size. This assessment is also evidenced by a comparison of the AFM images in terms of the particle size features with TEM size features for sub-monolayer assembly of the core-shell nanoparticles [26].

Depending on the thickness of the assembled film, the catalytic activation reveals a different degree in morphology changes. For the thicker film (Fig. 5A(b)), the particle size in the *x*–*y* plane appears larger after

Table 2
Roughness data based on the standard deviation (Rms) of *Z* values from the data in Fig. 5

	Thicker film (~7 layers of nanoparticles) (nm)	Thinner film (~3 layers of nanoparticles) (nm)
Before activation	Approx. 12.1	3.77
After activation	Approx. 14.5	2.88

activation, roughly equals the size for a collection of ~3 particles in the image of the unactivated particle assembly. For the thinner film (Fig. 5B(b)), there appears no significant change for the particle size after the activation, at least above the resolution limit due to the tip–sample convolution. In the *z*-direction, the height changes are, however, about the same for both films. The interparticle distance change is reflected by the appearance of smoother domains of nanoparticles after the activation. The porous morphology is also evident. As a rough estimate of the morphology change, the standard deviation (Rms) of the *Z* values for both films, shown in Table 2, was examined. For the thinner film, we detected a decrease of Rms, which seems to indicate a smoothing effect by the activation. For the thicker film, the change of Rms is relatively insignificant. There are two possible scenarios responsible for the morphological changes. One is the subtle increase in size of the assembled nanoparticles by interparticle fuse upon a complete removal of the networking dithiolates. The other is the formation of porous shell of the oxygenated species on the nanocrystal surfaces upon removal of the network shells. Although the data seem to support the presence of both possibilities, the issue of which one is predominant remains to be further investigated.

4. Conclusions

Taken together, the results have demonstrated that the shell reconstitution of the core-shell assembled gold nanoparticles upon the polarization of the film by an oxidative potential has played an important role in the catalytic activation. The partial or complete removal of the shell thiolates and dithiolates and the formation of the surface oxygenated gold species are responsible for the catalytic activity. Such a role

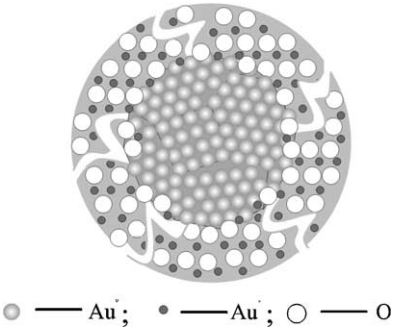

Scheme 1. A schematic illustration of the reconstituted core-shell structure showing the formation of pores and gold oxides.

has been discussed in a number of recent studies, including the incipient hydrous oxide/adatom mediator model [27]. The detected morphological change of the nanoparticles indicates that the size and interparticle distance can be effectively manipulated by these interfacial processes. The processes involved in the partial or complete desorption of network shells and the accompanying formation of the surface oxide film in the catalytic activation could also lead to the formation of porous morphology for the nanostructured catalysts. Scheme 1 illustrates schematically the reconstituted core-shell structure, which involves the formation of gold oxides and pores. While the role of oxide for gold catalysis has been discussed recently [12,27], the quantitative correlation of the interfacial structures and processes for our nanostructured catalysts is a subject of our in-depth investigation.

Acknowledgements

Financial support of this work is gratefully acknowledged from the ACS Petroleum Research Fund and SRF supplement, and the 3M Corporation. We thank Dr. S. Madan for donating some metal compounds.

References

[1] S. Wasmus, A. Küver, J. Electroanal. Chem. 461 (1999) 14.
[2] J. Lipkowski, P.N. Ross Jr. (Eds.), Electrocatalysis, Frontiers in Electrochemistry, vol. 5, VCH, New York, 1997.
[3] G.Q. Lu, A. Wieckowski, Curr. Opin. Coll. Interf. Sci. 5 (2000) 95.

[4] (a) S. Sriramulu, T.D. Jarvi, E.M. Stuve, J. Electroanal. Chem. 467 (1999) 132;
(b) E. Herrero, K. Franaszczuk, A. Wieckowski, J. Phys. Chem. 98 (1994) 5074.
[5] (a) C.E. Lee, S.H. Bergens, J. Phys. Chem. B 102 (1998) 193;
(b) U.A. Paulus, U. Endruschat, G.J. Feldmeyer, T.J. Schmidt, H. Bonnemann, R.J. Behm, J. Catal. 195 (2000) 383;
(c) T.J. Schmidt, H.A. Gasteiger, R.J. Behm, Electrochem. Commun. 1 (1999) 1;
(d) K.L. Ley, R.X. Liu, C. Pu, Q.B. Fan, N. Leyarovska, C. Segre, E.S. Smotkin, J. Electrochem. Soc. 144 (1997) 1543;
(e) M.E. Tess, P.L. Hill, K.E. Torraca, M.E. Kerr, K.A. Abboud, L. McElwee-White, Inorg. Chem. 39 (2000) 3942.
[6] G. Tremiliosi, H. Kim, W. Chrzanowski, A. Wieckowski, B. Grzybowska, P. Kulesza, J. Electroanal. Chem. 467 (1999) 143.
[7] S. Sriramulu, T.D. Jarvi, E.M. Stuve, Electrochim. Acta 44 (1998) 1127.
[8] (a) J.W. Long, R.M. Stroud, K.E. Swider-Lyons, D.R. Rolison, J. Phys. Chem. B 104 (2000) 9772;
(b) K.E. Swider, D.R. Rolison, Electrochem. Solid State Lett. 3 (2000) 4.
[9] M. Valden, X. Lai, D.W. Goodman, Science 281 (1998) 1647.
[10] P.C. Biswas, Y. Nodasaka, M. Enyo, M. Haruta, J. Electroanal. Chem. 381 (1995) 167.
[11] M. Hepel, J. Electrochem. Soc. 145 (1998) 124.
[12] (a) G.C. Bond, D.T. Thompson, Catal. Rev. 41 (1999) 319;
(b) G.C. Bond, D.T. Thompson, Gold Bull. 33 (2000) 41, and references therein.
[13] J.D. Aiken III, R.G. Finke, J. Mol. Catal. A: Chemical 145 (1999) 1.
[14] A.C. Templeton, W.P. Wuelfing, R.W. Murray, Acc. Chem. Res. 33 (2000) 27, and references therein.
[15] (a) M. Brust, M. Walker, D. Bethell, D.J. Schiffrin, R. Whyman, J. Chem. Soc., Chem. Commun. (1994) 801;
(b) M. Brust, J. Fink, D. Bethell, D.J. Schiffrin, C. Kiely, J. Chem. Soc., Chem. Commun. (1995) 1655.
[16] (a) F. Caruso, Adv. Mater. 13 (2001) 11, and references therein;
(b) J.J. Schneider, Adv. Mater. 13 (2001) 529;
(c) W. Schärtl, Adv. Mater. 12 (2000) 1899.
[17] (a) A. Sanchez, S. Abbet, U. Heiz, W.D. Schneider, H. Häkkinen, R.N. Barnett, U. Landman, J. Phys. Chem. A 103 (1999) 9573;
(b) U. Heiz, A. Sanchez, S. Abbet, W.D. Schneider, Chem. Phys. 262 (2000) 189.
[18] (a) M.J. Hostetler, J.E. Wingate, C.J. Zhong, J.E. Harris, R.W. Vachet, M.R. Clark, J.D. Londono, S.J. Green, J.J. Stokes, G.D. Wignall, G.L. Glish, M.D. Porter, N.D. Evans, R.W. Murray, Langmuir 14 (1998) 17;
(b) M.J. Hostetler, C.J. Zhong, B.K.H. Yen, J. Anderegg, S.M. Gross, N.D. Evans, M.D. Porter, R.W. Murray, J. Am. Chem. Soc. 120 (1998) 9396;
(c) M.J. Hostetler, A.C. Templeton, R.W. Murray, Langmuir 15 (1999) 3782;
(d) A.C. Templeton, M.J. Hostetler, C.T. Krsft, R.M. Murray, J. Am. Chem. Soc. 120 (1998) 1906.
[19] M.M. Maye, Y.B. Lou, C.J. Zhong, Langmuir 16 (2000) 7520.
[20] (a) Y.B. Lou, M.M. Maye, L. Han, J. Luo, C.J. Zhong, Chem. Commun. (2001) 473;
(b) J. Luo, Y.B. Lou, M.M. Maye, C.J. Zhong, M. Hepel, Electrochem. Commun. 3 (2001) 172.
[21] M. Hepel, in: A. Wieckowski (Ed.), Interfacial Electrochemistry: Theory, Experiments and Applications, Marcel Dekker Inc., New York, 1999, p. 599.
[22] (a) F.L. Leibowitz, W.X. Zheng, M.M. Maye, C.J. Zhong, Anal. Chem. 71 (1999) 5076;
(b) L. Han, M.M. Maye, F.L. Leibowitz, N.K. Ly, C.J. Zhong, J. Mater. Chem. 11 (2001) 1258.
[23] (a) C.D. Bain, E.B. Troughton, Y.T. Tao, J. Evall, G.M. Whitesides, R.G. Nuzzo, J. Am. Chem. Soc. 111 (1989) 321;
(b) H. Sellers, A. Ulman, Y. Shnidman, J.E. Eilers, J. Am. Chem. Soc. 115 (1993) 9389.
[24] F. Brouers, J.P. Clerc, G. Giraud, J.M. Laugier, Z.A. Randriamantany, Phys. Rev. B 47 (1993) 666.
[25] (a) M.D. Musick, C.D. Keating, M.H. Keefe, M.J. Natan, Chem. Mater. 9 (1997) 1499;
(b) M.D. Musick, D.J. Pena, S.L. Botsko, T.M. McEvoy, J.N. Richardson, M.J. Natan, Langmuir 15 (1999) 844.
[26] L. Han, M.M. Maye, C.J. Zhong, in: S.J. Stranick, P. Searson, L.A. Lyon, C.D. Keating (Eds.), Anisotropic Nanoparticles—Synthesis, Characterization, and Applications, Materials Research Society, 2001, Vol. 635, C4.5.
[27] L.D. Burke, P.F. Nugent, Gold Bull. 31 (1998) 39.